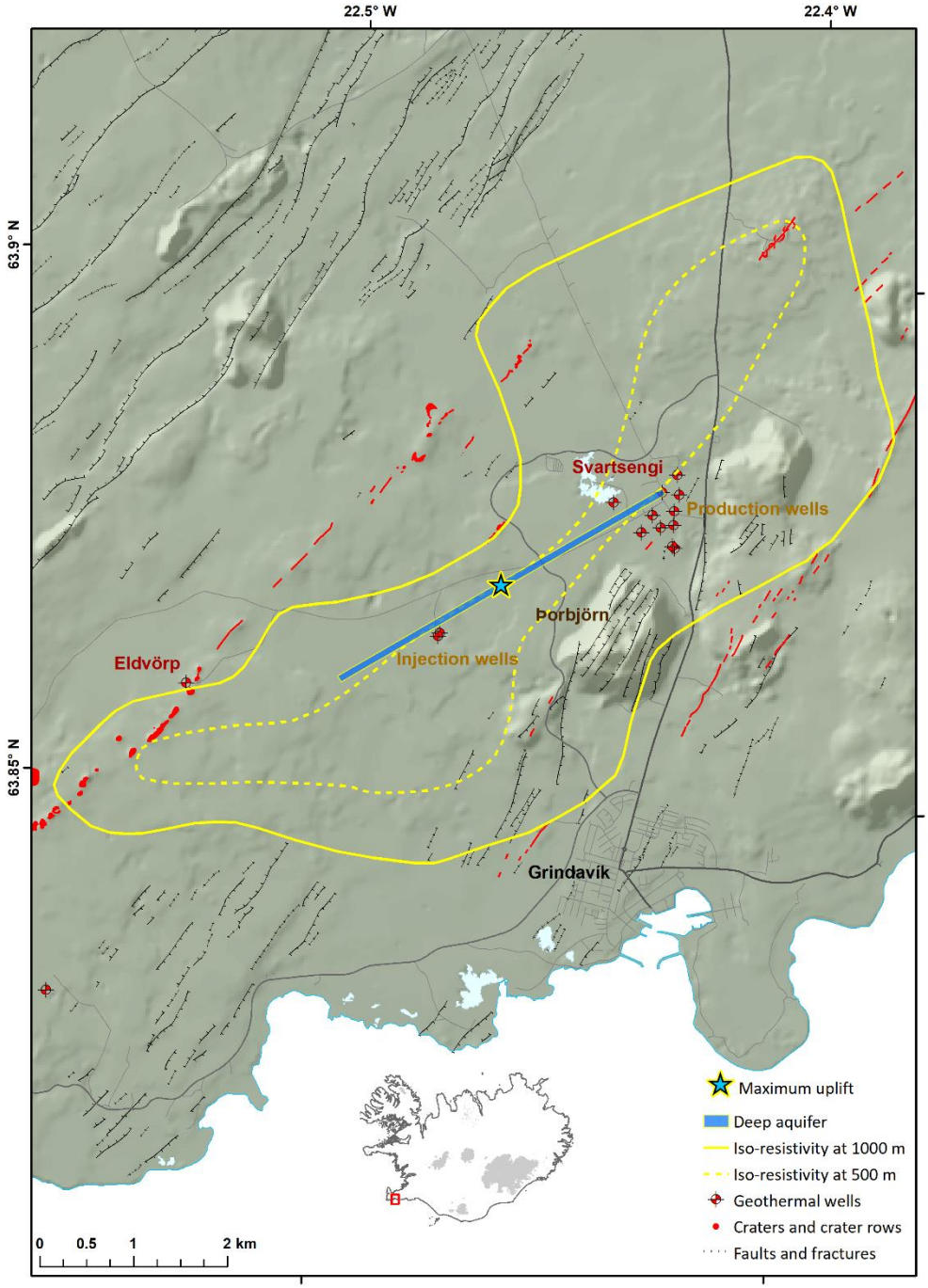

Fig. S1. Close up map of the Svartsengi high temperature field. The red lines denote postglacial eruption fissures. The yellow lines show the top of the resistive core at 0.5 and 1.0 km depth according to TEM resistivity measurements [12] defining the top of the geothermal reservoir. The thin, blue rectangle shows the location of the proposed inflated aquifer at 4 km depth according to the poroelastic model, while the centre of uplift is shown as a blue star and red circles with crosses are geothermal wellheads. Note how the proposed aquifer is located below the geothermal field and follows its main direction.

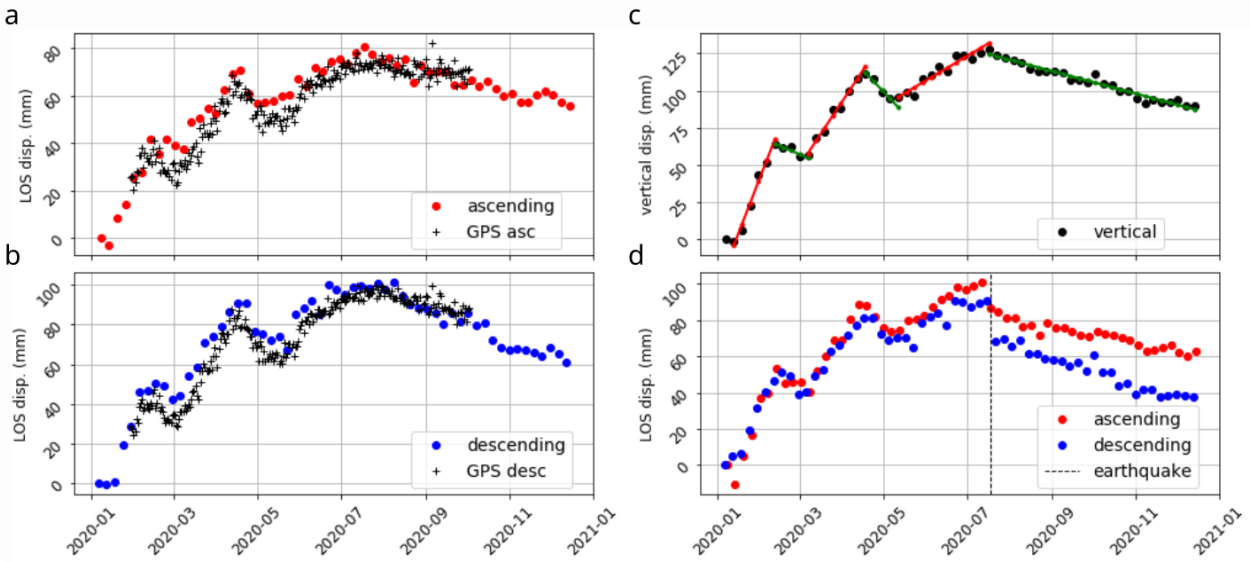

Fig. S2 InSAR ascending (a) and descending (b) LOS time-series compared to GNSS data (black cross); (c) Vertical displacement obtained by 2D decomposition of the two LOS directions for the total maximum uplift registered on 17/07/2020: red and green lines show the linear interpolation of the single uplift and subsidence episodes; (d) ascending and descending LOS time-series over the area of the 18th July 2020 earthquake, showing that a new subsidence phase started after the earthquake.

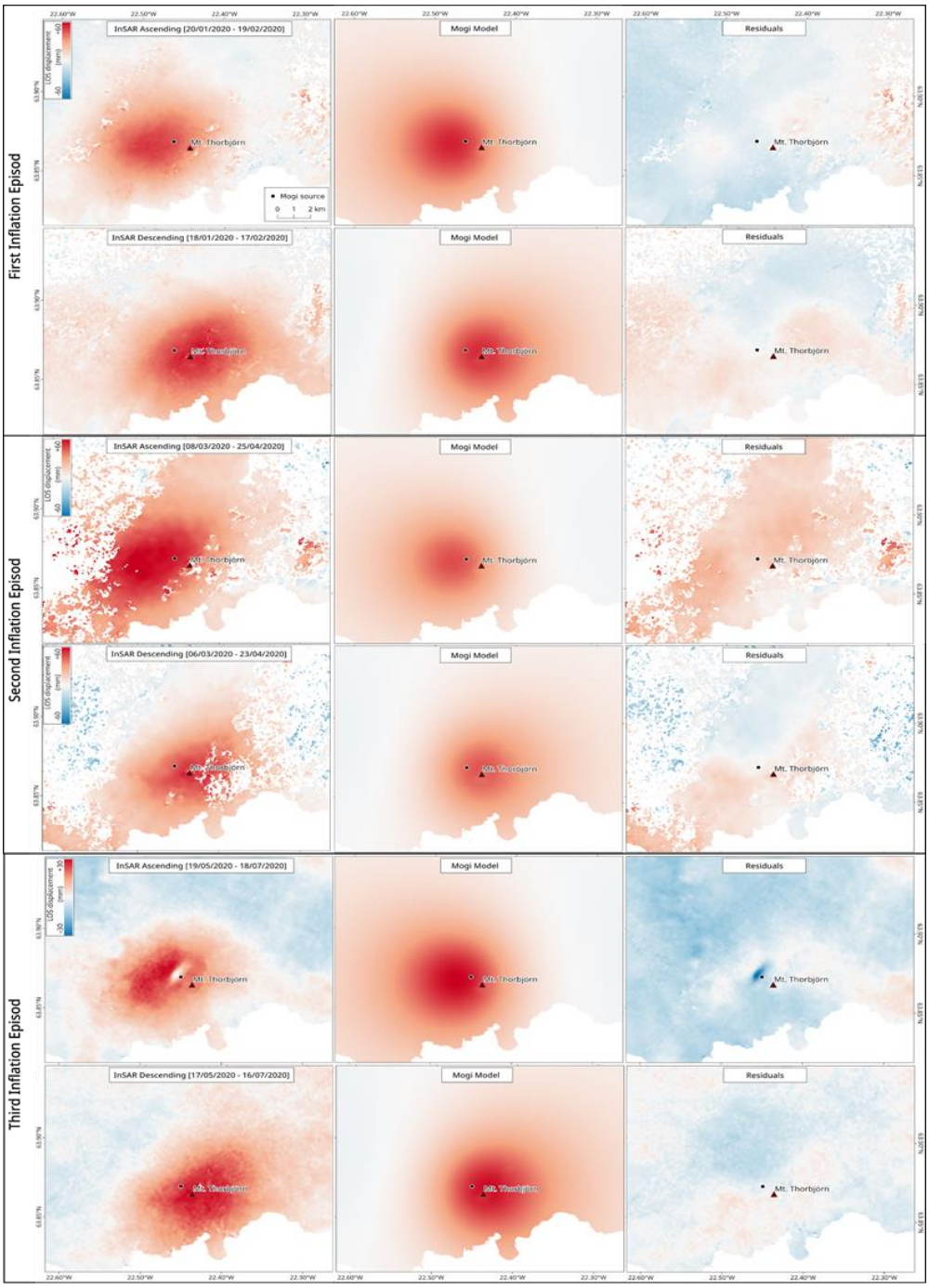

Fig. S3. InSAR data and Mogi point source model simulation. First column shows the unwrapped cumulative displacement for each inflation episode. Second column shows the modelled displacement. Third column shows the model residual, estimated as the difference between the InSAR observations and the model. For each episode there are two rows of datasets for ascending (first row) and descending (second row) geometries. Black dot shows the horizontal location of the Mogi source. The rectangle shows the location of Mt. Thorbjörn.

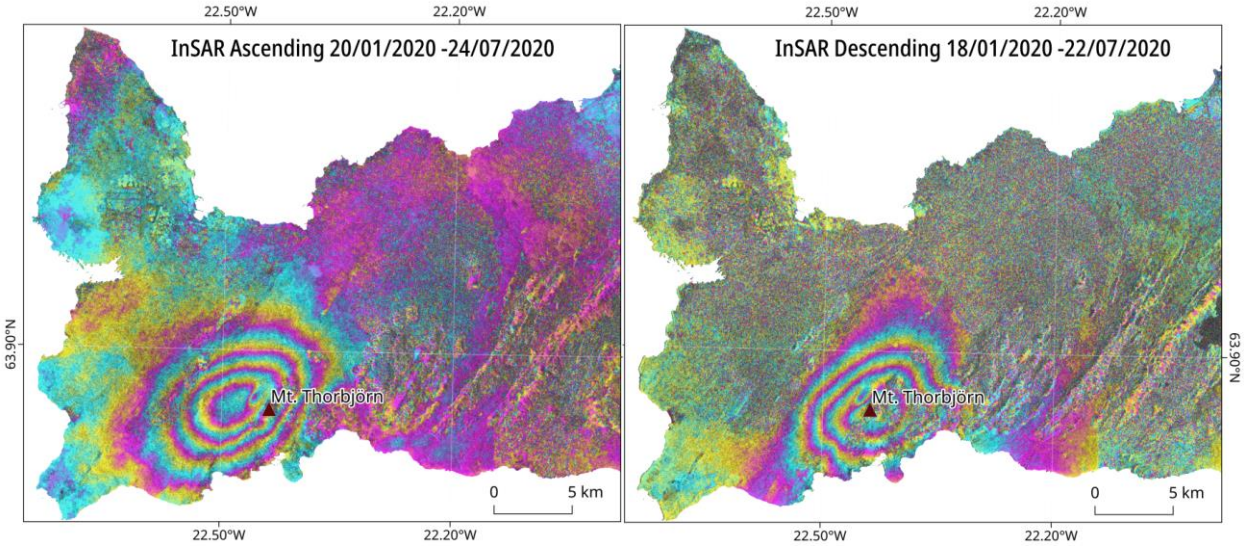

Fig. S4. Long-term (7-months) wrapped interferograms showing the extent of the inflated area. Four fringes are visible in both ascending (left side) and descending (right side) geometries. One fringe corresponds to a LOS displacement of approximately 2,8 cm (C-band radar sensor), therefore 4 fringes correspond to approximately 11 cm of LOS displacement. The triangle shows the location of Mt. Thorbjörn.

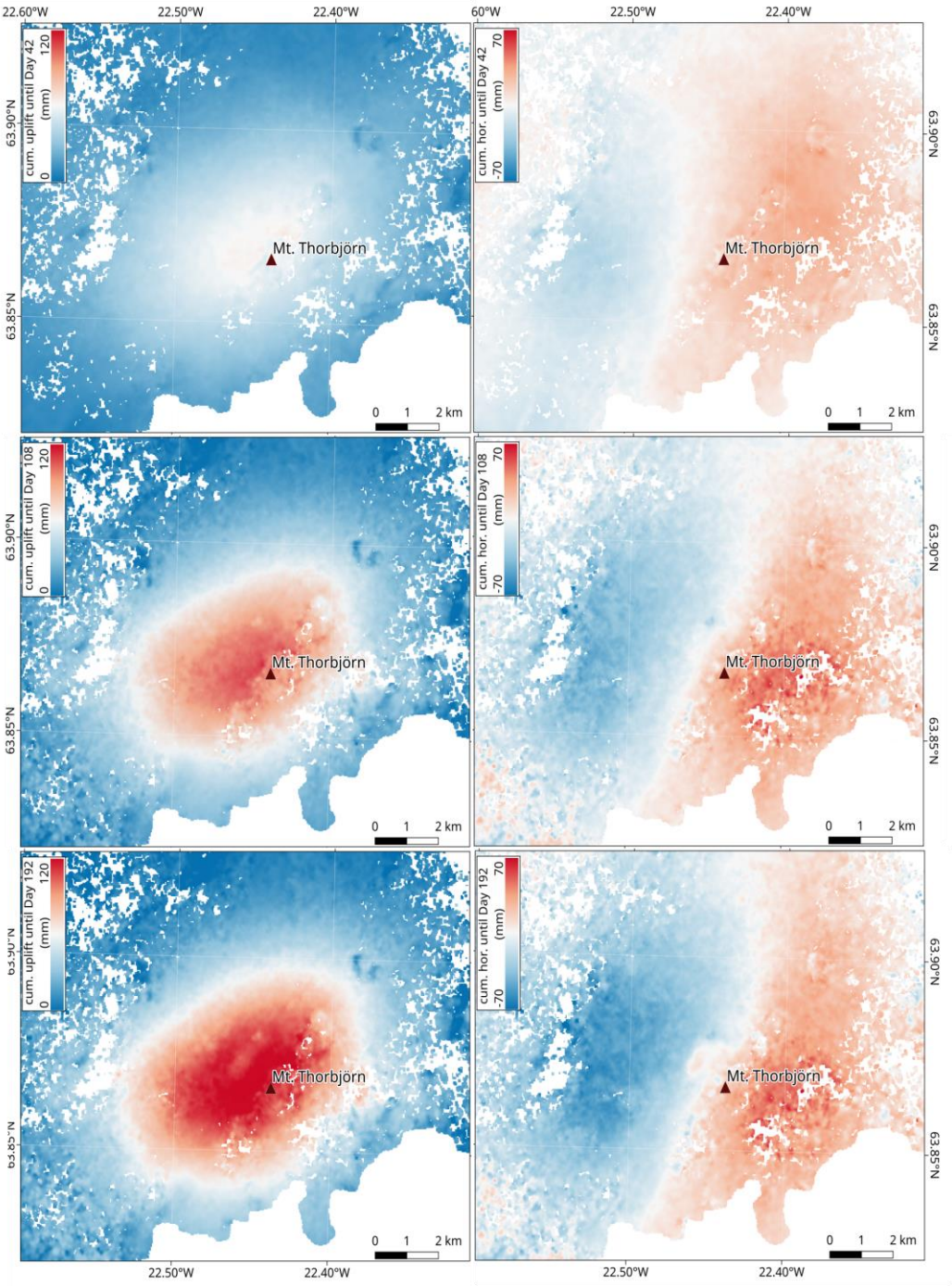

Fig. S5. Vertical (first column) and horizontal (second column) cumulative displacement maps showing the cumulative displacement after each uplift episode: first row for the period 07/01 – 18/02/2020; second row for the period 07/01/2020 – 24/04/2020; third row for the period 07/01 – 17/07/2020. Positive values correspond to an uplift in the vertical maps and to an eastward movement in the horizontal maps. The triangle shows the location of Mt. Thorbjörn

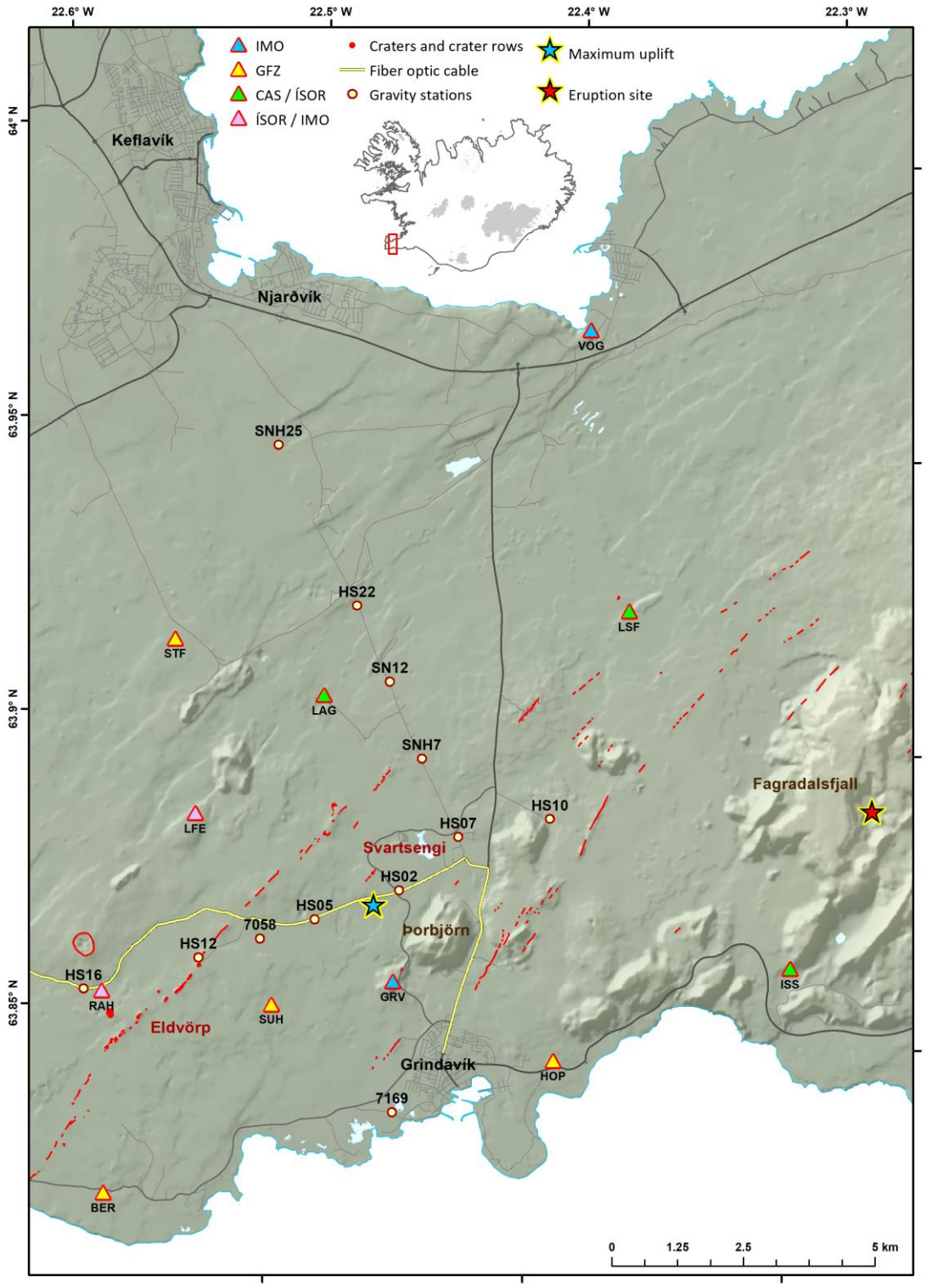

Fig. S6. The locations of gravity stations are marked with yellow circles. The centre of uplift is shown as a blue star, in between stations HS02 and HS05. The stations HS10 and 7058 were not measured in January 2020. The red lines show postglacial eruption fissures, while the red star shows the 2021 eruption site. Triangles denote seismic stations and the yellow line the location of the DAS cable.

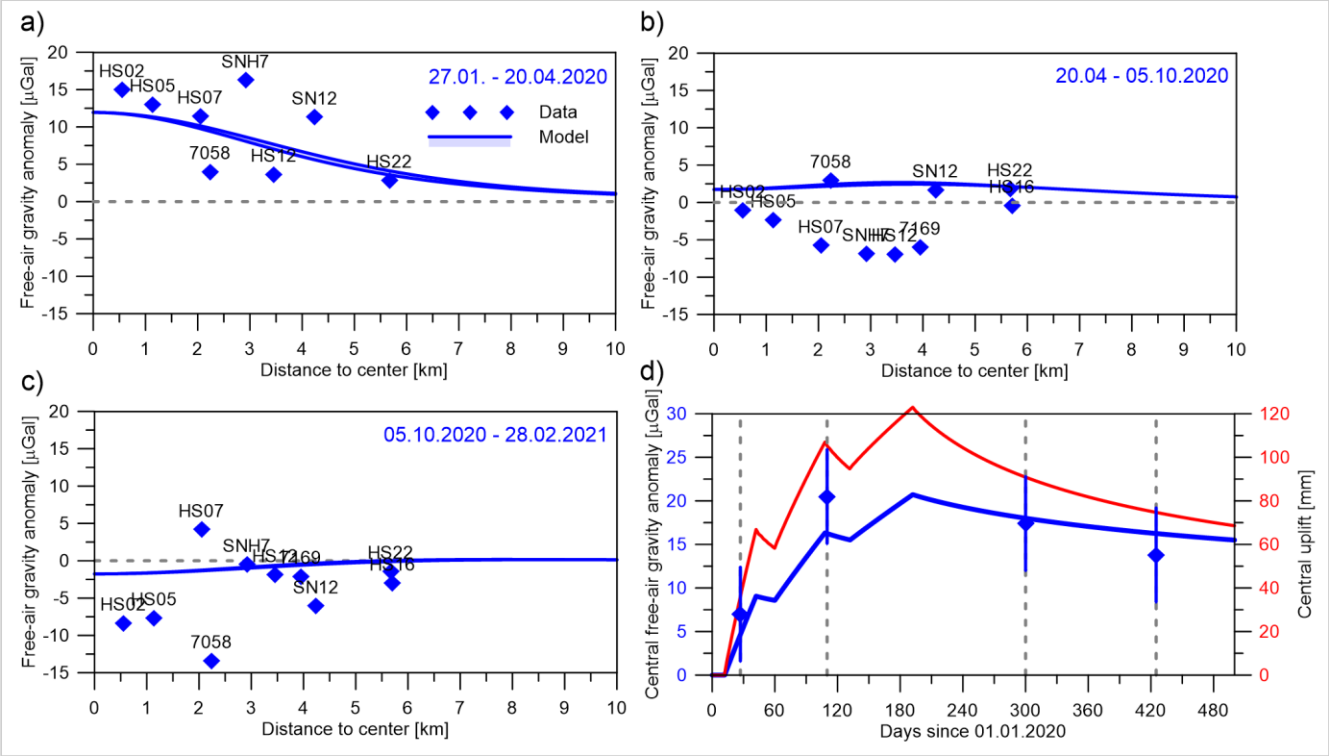

Fig. S7. a-c) Free-air gravity anomalies from the complete campaign measurements (diamonds) used in this study, in comparison with the model predictions shown by the double blue curves (along the major and minor axes of the elliptic uplift pattern). Note that a correction for the long-term trend is applied to the data. The trend is estimated to be location-dependent and proportional to the episodic uplift, with the maximum of -5 µGal/year. d) Temporal variation of free-air gravity anomaly (diamonds) averaged from the campaign data of stations HS02 and HS05 in comparison of the model prediction (blue curve) for the uplift centre. The error bars (+/-5.4 µGal) represent the standard deviation of the model to the data. The red curve shows the theoretical central uplift.

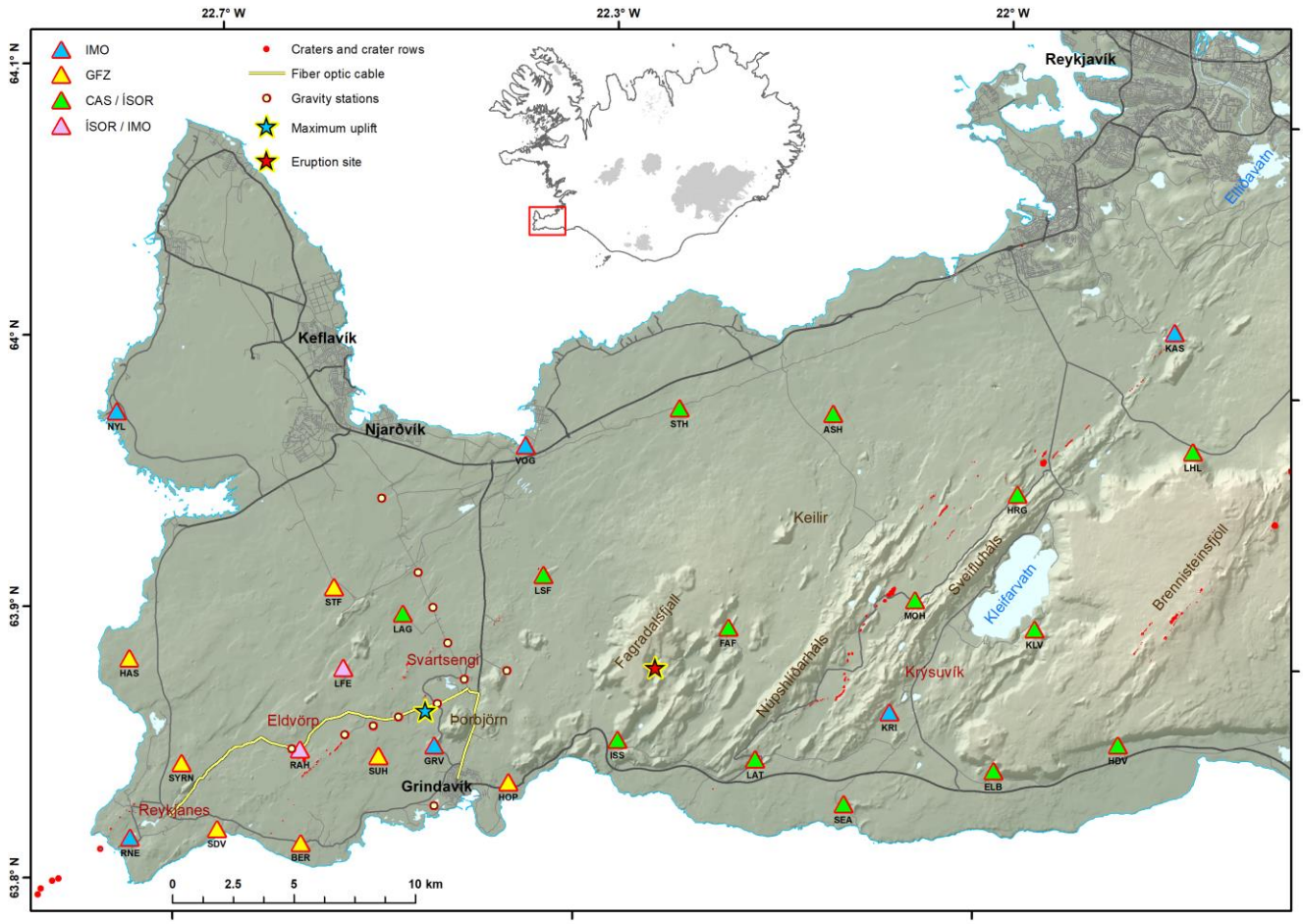

Figure S8. Overview of the seismic and gravity stations on the Reykjanes Peninsula. The seismic stations marked in blue are a part of the national seismic network in Iceland (SIL network) operated by IMO, in yellow are stations deployed by GFZ, in green are stations from the Czech Academy of Sciences operated together with ÍSOR, and in pink are joint ÍSOR-IMO stations. The yellow circles denote the gravity stations, and the blue and red stars show the centre of uplift and the 2021 eruption site in the Fagradalsfjall mountain complex, respectively. The DAS cable from the Mila Telecommunication Company is shown as yellow line. 26 of the seismic stations were used together with the DAS data to create a new catalogue for the period February 1st to August 30th, 2020.

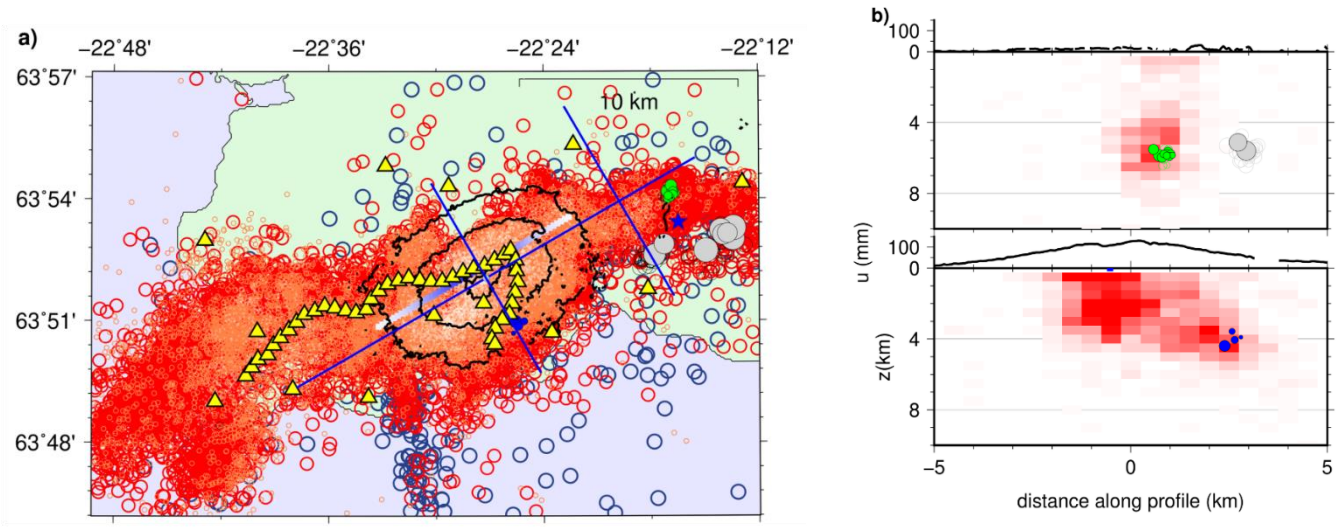

Figure S9. **a.** Earthquakes located between February and August 2020 using the combined network of permanent and temporary seismic stations (yellow triangles) and virtual stations along the DAS cable (yellow triangles in linear arrangement). Earthquakes between 0-2 km, 2-4km, 4-10 km and below 10 km depth are plotted as white, orange, red and blue open circles, respectively. The earthquake swarms in November and December 2019 are plotted as green and gray filled circles, respectively. Earthquakes between 20-22 January 2020 are plotted as blue filled circles. The cross-sectional NE-SW profile of Fig. 4 is plotted as a blue line. The cross sections along two crossing NW-SE profiles are shown in b. The black contour lines indicate the shape of the uplift pattern measured in April 2020. The linear source model is indicted as blue bar. **b.** Earthquakes within +/- 1 km along the two crossing profiles were gridded and are plotted as event density. See Fig. 4 to translate color legend. The projected uplift profile is plotted above the cross sections.

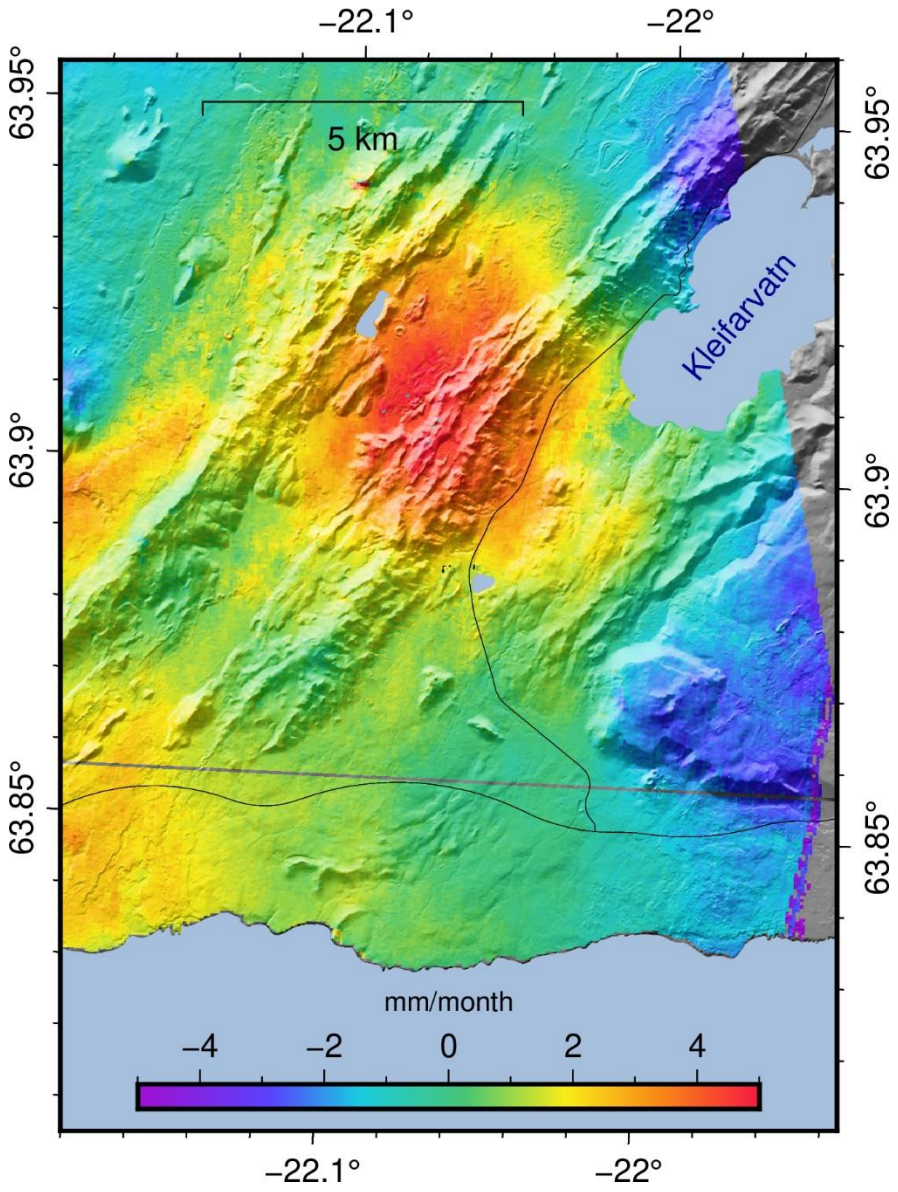

Figure S10. Average monthly vertical velocities at Krýsuvík between the 3rd of August and the 10th of November 2020. Velocities were estimated by decomposing the line-of-sight signal of the InSAR time-series analysis of Sentinel-1 images from ascending track T16 and descending track T155. Background shows shaded topography and roads (black lines).

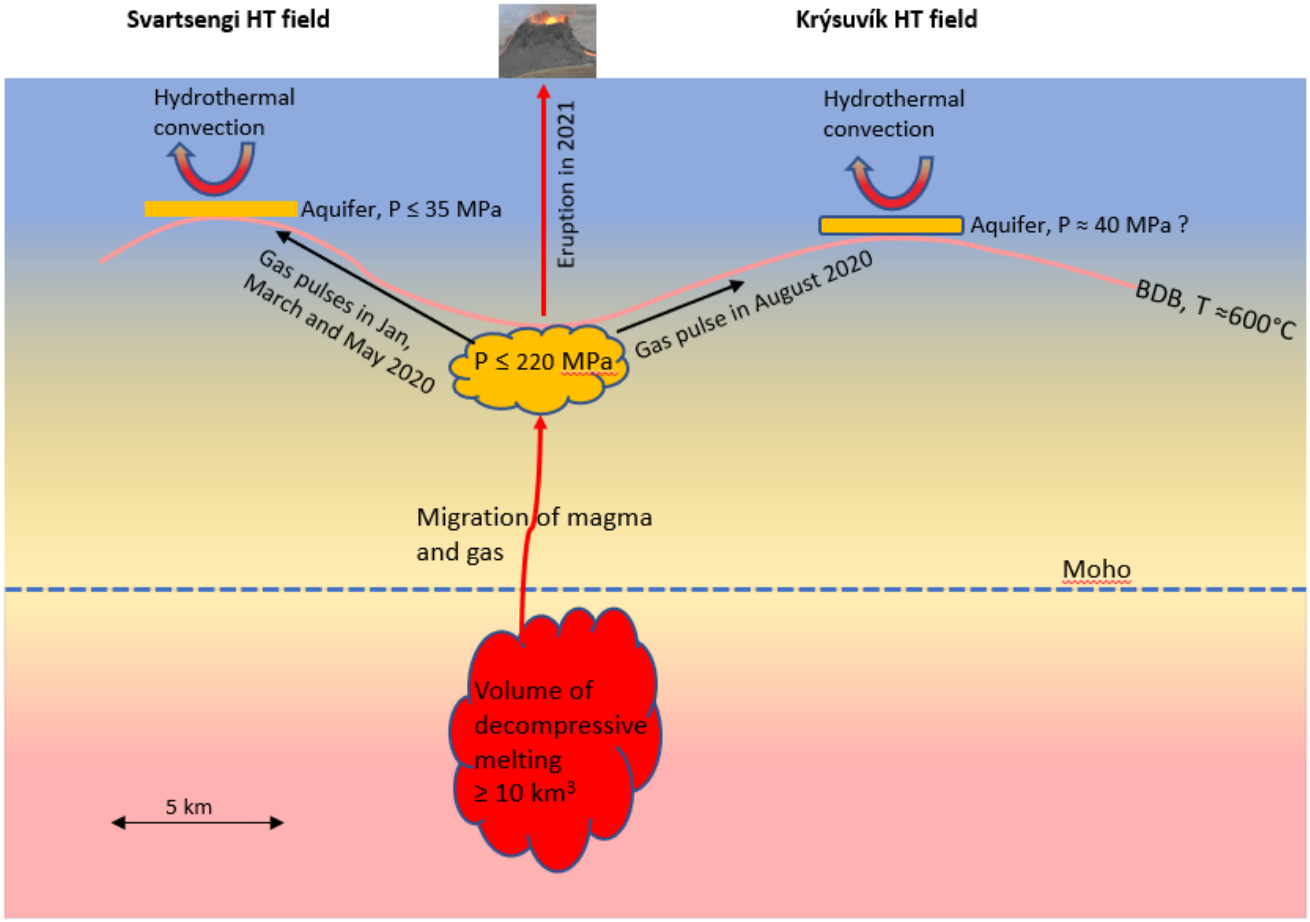

Figure S11. A conceptual model of the processes leading to the uplift, seismic unrest, and the volcanic eruption. Magma and gas migrate upwards from a decompressive melting beneath Moho and becomes trapped at the brittle-ductile boundary (BDB). When the gas pressure has reached certain critical value at the BDB, batches of CO_2 are driven along the BDB towards the underpressurized geothermal aquifers where it intrudes and inflates the overburden. The suggested amount of subcrustal magma is based on the degassing process (SI 2). Vertical and horizontal scales are the same.

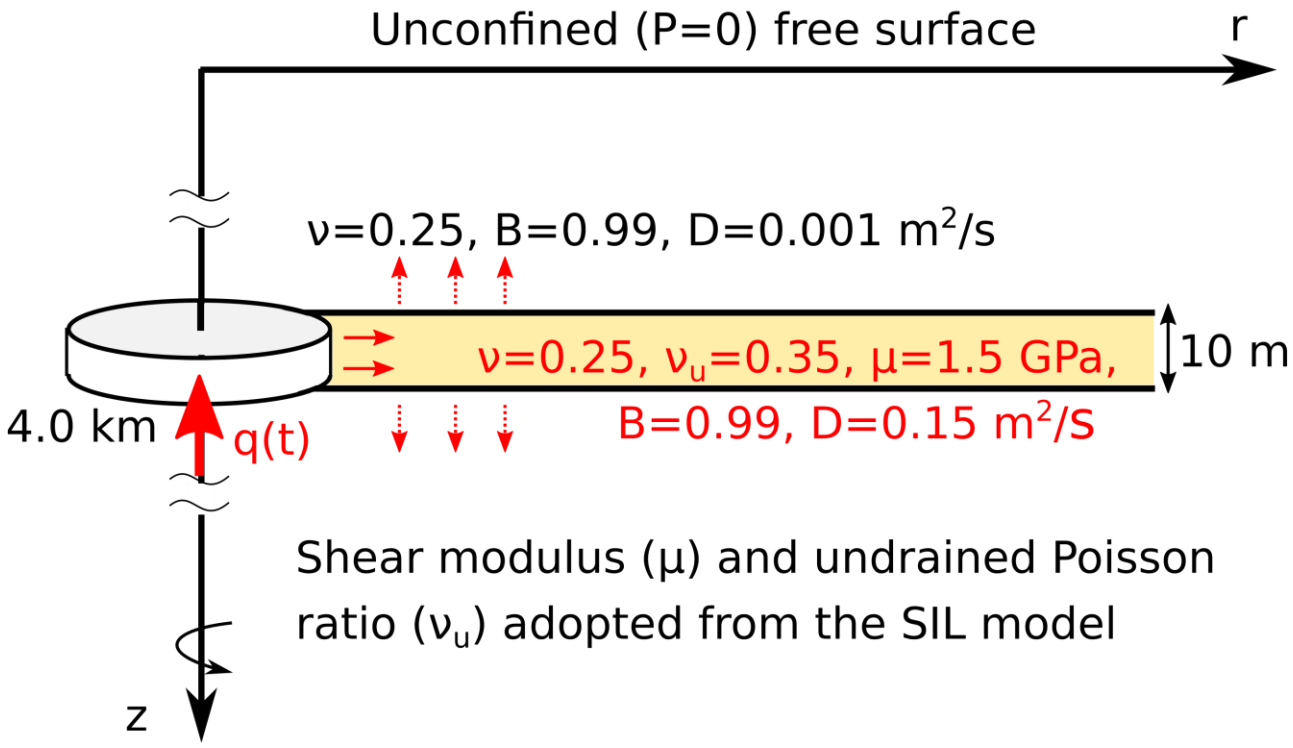

Figure S12. A sketch of the multi-layered poroelastic structure model used in this study. The medium in each poroelastic layer is defined by 5 parameters: the shear rigidity (μ), the drained and undrained Poisson ratios (ν, ν_u), the Skempton coefficient (B) and the hydraulic diffusivity (D). Based on the assumption that seismic waves propagate under undrained conditions, the seismic reference model SIL (Stefánsson et al., 1993) is adopted to define the elastic parameters μ and ν_u and their layering in the present poroelastic structure. Outside the thin aquifer layer, which is inserted into the SIL structure at the depth of 4 km, all poroelastic layers have the uniform values for parameters ν, B and D.

Gravity:	**Values for central points: HS-02, HS-05 and HS-07**		
End of Jan=0	**April 22-28th 2020**	**October 5-6th 2020**	**February 16-18th 2021**
HS-02	13.9	10.3	0.3
HS-05	12.0	7.4	-1,8
HS-07	10.6	2.9	5.8
Average at centre of uplift	**12.2**	**6.9**	**1.4**
Corrected for January uplift	19.2	13.9	8.4
Background corrected	20.5	17.4	13.8
Elevation:	**Value for central points: HS-02, HS-05 and HS-07**		
End of Jan=0	**April 22-28th 2020**	**October 5-6th 2020**	**February 16-18th 2021**
HS-02	0.0775	0.0724	0.0335
HS-05	0.0682	0.0790	0.0589
HS-07	0.0669	0.0743	0.0544
Average at centre of uplift	**0.0709**	**0.0752**	**0.0489**
4 cm added	0.1109	0.1152	0.0889
µGal/m	172	0	207

Table S1. Gravity changes in µGal and elevation changes in m at the centre of uplift for the three different time periods between the gravity campaigns. All values refer to changes form the first campaign on at January 28th-29th where the uplift was already 4 cm. Scintrex CG-5 AutoGrav gravity meter was used. At each station we made 3-4 readings with a few minutes' interval, each consisting of the average of 6 automatic readings per second over 60 seconds where outliers were automatically removed. The variability of the 3-4 readings where of the order of a few µGal and the average value was used as the outcome. Then the same procedure was used back and forth from one station to another to create a closed measurement loop to estimate and correct for instrumental drift. Therefore, each station was measured several times during each campaign and the average value used as the final gravity value at each station.

Table S2: Parameters used for the Lassie waveform-based detection and location.

Grid dimension	40 km x 40 km x 15 km	Sampling rate	200 Hz
Grid spacing	500 m	Waveform filtering	3 – 25 Hz
STA/LTA (P)	0.2 s / 1.6 s	Smoothing duration	2 s (P and S)

Table S3: Velocity model implemented in the Lassie waveform-based detection and location.

Depth (km)	Vp (km/s)	Vs (km/s)	Density (kg/m^3)	Comment / description
0.0	3.600	1.800	0.900	Fresh basalt and/or hyaloclastite
0.5	3.600	1.800	0.900	
0.5	4.000	2.245	2.340	
1.0	4.000	2.245	2.340	
1.0	4.815	2.705	2.470	Downward increasing alteration and compaction
2.0	4.815	2.705	2.470	
2.0	5.380	3.025	2.670	
3.0	5.380	3.025	2.670	
3.0	5.785	3.250	2.820	
4.0	5.785	3.250	2.820	
4.0	6.095	3.425	2.880	
5.0	6.095	3.425	2.880	
5.0	6.365	3.575	2.890	Oceanic layer 3 ?
6.0	6.365	3.575	2.890	
6.0	6.568	3.683	2.895	Oceanic layer 3
7.0	6.568	3.683	2.895	
7.0	6.615	3.715	2.900	
8.0	6.615	3.715	2.900	
8.0	6.673	3.748	2.910	
9.0	6.673	3.748	2.910	
9.0	6.750	3.792	2.917	
10.0	6.750	3.792	2.917	
10.0	6.890	3.871	2.923	
12.0	6.890	3.871	2.923	
12.0	6.950	3.904	2.930	
14.0	6.950	3.904	2.930	
14.0	7.010	3.938	2.937	
16.0	7.010	3.938	2.937	Sub Moho
16.0	7.065	3.969	2.944	
18.0	7.065	3.969	2.944	
18.0	7.120	4.000	2.950	
20.0	7.120	4.000	2.950	
20.0	7.175	4.031	3.080	
24.0	7.175	4.031	3.080	
24.0	7.260	4.079	3.100	
28.0	7.260	4.079	3.100	
28.0	7.350	4.130	3.120	
32.0	7.350	4.130	3.120	

IS1: A short derivation of the theory of the buoyancy-driven, pulsating outflow from a deep reservoir

This short information sheet (IS) is inserted as supplementary material to the paper by Flovenz et al. "*Episodic unrest at the Svartsengi hydrothermal field - an example of magma-fluid interaction heralding a coming eruption*", and refers to figs. 4 and 5 in the main text.

The problem is similar to the gravity-driven outflow from a tank drained through a siphon under viscous, laminar flow (e.g. Loiacono, 1987; Bird et al., 2002). One difference is that the driving potential due to water pressure at the bottom of the tank is replaced by an overpressure under the roof of the sealed reservoir, which is generated by the accumulation of a fluid of lower density below the seal of the reservoir. The problem is described by two coupled differential equations, the conservation of mass (linear momentum) and the energy balance between driving and resisting forces during flow.

The problem geometry is shown in Fig. 5a of the maintext and solutions are derived below. Interestingly, the volume flux in the end member cases depends only on the initial flux and a decay time t_0 which depends on the ratio between the reservoir and channel size and the initial reservoir thickness. They are suited for discussing end member geometries, as all other solutions are in between the two end member cases.

The theory is an adaption of the gravity-driven depletion of a tank to the problem of buoyancy-controlled depletion of a fluid reservoir at depth by laminar, viscous channel or pipe flow. The reservoir at depth is approximated by a circular disc of radius r and thickness $h_2 = h_2(t)$ (Fig. 5a). The thickness h_2 is determind by the thickness of the supercritical fluid column. If the fluids density ρ_f is smaller than the density of the surrounding rocks or magma beneath (both set to ρ_m), an overpressure can develop at the roof of the reservoir of $\Delta P = (\rho_m - \rho_f)gh_2 = \Delta\rho g h_2$. If the pressure at the top of the channel (at the top of the brittle ductile zone) is set to P_1, the pressure at the roof of the reservoir at depth (entry point to the channel) is (see Fig. 5a)

$$P_2(t) \;\; = \;\; P_1 + \rho_m g h + \Delta\rho g h_2(t)\,.$$

This pressure difference can drive flow though the channel until the reservoir is depleted and $h_2(t) \to 0$. If during depletion the channel would be steadily open over a vertical length of $h_f = h + h_2(t)$, the overpressure is larger and controlled by $\Delta\rho g h_f(t)$. However, as discussed below, the channel flow might

be discontinous from a fracture mechanical point of view (e.g. Dahm, 2000), which can be considered by an overpressure valve mechanism.

We first assume laminar flow through an open channel (pipe) of constant radius of c with time dependent velocity $v(t)$ (or volume flux $q(t) = \pi c^2 \cdot v(t)$) and ask the question how long it takes until the reservoir is emptied and how the q changes with time. The conservation of mass (linear momentum, ρ_f unchanged) is given by

$$q(t) \;=\; \pi r^2 \frac{dh_f}{dt} \;=\; -\pi c^2 v(t) \quad \text{or} \quad \frac{dh_f}{dt} \;=\; -\frac{c^2}{r^2} v(t)\,.$$

It is convenient in fluid mechanics to express all variables in dimensionless form by e.g. $\hat{h} = h_f/h_0$, $\hat{v} = v/v_0$ and $\hat{t} = t/t_0$, where h_0 and v_0 are measured at time $t = 0$. The dimensionless form of the conservation of mass is

$$\frac{h_0}{t_0}\frac{d\hat{h}}{d\hat{t}} \;=\; -\frac{c^2}{r^2} v_0 \hat{v}(t) \quad \text{or} \quad \frac{d\hat{h}}{d\hat{t}} \;=\; -\hat{v}(t)\,, \tag{IS1.1}$$

with decay time $t_0 = \dfrac{r^2 h_0}{c^2 v_0} = \pi \dfrac{r^2 h_0}{q_0}$. For instance, if in the example given in Fig. 5 the thickness h_2 of the accumulated overcritical volatiles at the upper end of a magmatic sill-like intrusion is initially in the range of $h_0 = 50\,m$, the lateral extent of the sill-shaped reservoir would be in the range of $2r = 900\,m$.

The second equation balances the potential energy (pressure) from the driving overpressure with the pressure needed to sustain laminar viscous flow and the kinetic component from the movement of fluid mass. If needed, an additional component to overcome a velocity-independent force can be added, but is neglected here. Acceleration effects can be discarded (quasi-steady state approach, see e.g. Bird et al., 2002, pp. 200-229) The equation is known as the modified Bernoulli equation and is in our case

$$\begin{aligned}
\frac{\rho_f}{2} v(t)^2 + \frac{8\rho_f \nu L}{c^2} v(t) \;=\; P_2(t) - P_1 \;&=\; \Delta\rho g h_f(t) \qquad \text{(IS1.2)}\\
v(t)^2 + \frac{16\nu l}{c^2} v(t) - \frac{2\Delta\rho g}{\rho_f} h_f(t) \;&=\; 0\\
v_0^2 \hat{v}(t)^2 + \frac{16\nu l}{c^2} v_0 \hat{v}(t) - \frac{2\Delta\rho g}{\rho_f} h_0 \hat{h}(t) \;&=\; 0\\
v_0^2 \hat{v}(t)^2 + \frac{16\nu l}{c^2} v_0 \hat{v}(t) - \left\{ v_0^2 + \frac{16\nu l}{c^2} v_0 \right\} \hat{h}(t) \;&=\; 0\\
\hat{v}(t)^2 + \frac{16\nu l}{c^2}\frac{1}{v_0} \hat{v}(t) - \left\{ 1 + \frac{16\nu l}{c^2}\frac{1}{v_0} \right\} \hat{h}(t) \;&=\; 0
\end{aligned}$$

$$\hat{v}^2(t) + 2b\hat{v}(t) - \{1+2b\}\,\hat{h}(t) \;=\; 0\,,$$

where $\dfrac{2\Delta\rho g}{\rho_f}h_0 = v_0^2 + \dfrac{16\nu l}{c^2}v_0$ and $b = \dfrac{8\nu l}{c^2 v_0}$ has been used. ν is the kinematic viscosity and L is length of the open section of the channel (Fig. 5a). Interestingly, the modified dimensionless Bernoulli equation depends only on one dimensionless parameter b, which is a function of viscosity and channel length and the initial reservoir height and flow velocity.

The two coupled differential equations in (IS1.1),

$$\frac{d\hat{h}}{d\hat{t}} \;=\; -\hat{v} \quad \text{and} \quad \hat{v} \;=\; -b \pm \sqrt{b^2 + (1+2b)\,\hat{h}}\,, \tag{IS1.3}$$

can solved by insertion of the second into the first equation which leads to a single ordinary differential equation as

$$\frac{d\hat{h}}{d\hat{t}} \;=\; b - \sqrt{b^2 + (1+2b)\hat{h}}\,, \tag{IS1.4}$$

where the negative sign was omitted.

We analyse two end member models where either $b \to 0$ or $b \to \infty$. The first case is realised if e.g. the viscosity ν is zero, leading to

$$\frac{d\hat{h}}{d\hat{t}} = -\sqrt{\hat{h}} \quad \text{with solution} \quad \hat{h}(\hat{t}) \;=\; \left(1 - \frac{\hat{t}}{2}\right)^2 .$$

This is the well known Torricelli solution for the outflow of a tank. **The time to deplete the reservoir is finite** and given by $t_{\text{dep}} = 2t_0$. The velocity is equated from (IS1.3) to

$$v(t) \;=\; v_0\left(1 - \frac{t}{2t_0}\right) \quad \text{with} \quad 0 \le t \le 2t_0\,.$$

The second case is realised if viscosity is non-zero and $L \gg c$. It leads to

$$\frac{d\hat{h}}{d\hat{t}} \;=\; b - b\sqrt{1 + \frac{1}{b^2}\,(1+2b)\,\hat{h}} \;\approx\; b - b\left(1 + \frac{1}{b}\hat{h} + \frac{1}{2b^2}\hat{h} \pm \cdots\right) = -\hat{h}$$

with solution

$$\hat{h}(\hat{t}) \;=\; e^{-\hat{t}} \quad \text{or} \quad h_f(t) \;=\; h_0 e^{-t/t_0}\,. \tag{IS1.5}$$

If the channel flow is dominated by viscous pressure drag the reservoir will never be finally depleted. All other solutions are in between these two extreme cases. The velocity, and thus the flux of fluid, is equated from (IS1.3) and is for the viscosity-dominated depletion given by

$$v(t) \;=\; \frac{v_0}{h_0} h_f(t) \;=\; v_0 e^{-t/t_0} \quad \text{with} \quad t \geq 0\,. \tag{IS1.6}$$

References

Bird, R., Steward, W., & Lightfoot, E., 2002. *Transport phenomena*, 2nd edition, John Wiley & Sons, New York, NY.

Dahm, T., 2000. On the shape and velocity of fluid-filled fractures in the earth, *Geophys. J. Int.*, **142**, 181–192.

Loiacono, N. J., 1987. Time to drain a tank with piping, *Chemical Engineering*, **94**(11), 164–166.

IS 2. A short note on the amount of subcrustal degassed melt beneath the eruption site in Fagradalsfjall

This short information sheet (IS) is inserted as supplementary material to the paper by Flóvenz et al. ”Episodic unrest at the Svartsengi hydrothermal field - an example of magma-fluid interaction heralding a coming eruption”,

The result of the poroelastic model shows that a total of $9.5 \cdot 10^7$ m^3 of CO_2 intruded the roots of the Svartsengi high temperature field in three batches of similar size. If we assume that similar amount of CO_2 was intruded into the Krýsuvík high temperature field in the fourth batch from the same source of melting, we can conclude that the total amount of CO_2 that has left the source of melting and intruded the roots of the two high temperature fields is close to $13 \cdot 10^7$ m^3.

Assuming the density of this volume to be 840 kg/m^3 the total intruded mass is $1.1 \cdot 10^{11}$ kg.

In a paper by Stephen Self et al. (2005) the authors estimate that 13 Mt ($13 \cdot 10^9$ kg) could be released for every km^3 of basaltic lava erupted provided 100% degassing of the melt. This allows us to calculate the corresponding volume of melt that must be 100% degassed to produce the intruded volume of CO_2 into the roots of the Svartsengi and Krýsuvík hight temperature fields:

Volume of generated melt = $1.1 \cdot 10^{11}$ kg_{CO2} / $1.3 \cdot 10^{10}$ kg/m^3_{melt} = 8.5 km^3

If the density of the CO_2 is overestimated, it will reduce the melt volume. On the contrary, we will hardly ever have 100% degassing of the subcrustal magma which means that the volume of melt must be substantially greater. It can be concluded that the result of the poroelastic modelling indicates that a magma source of the order of 10 km^3 at least must already exist just below Moho.

This is a huge volume compared to the present estimated eruption rate of ~12 m^3/s at Mt. Fagradalsfjall in June 2021. Therefore, we can conclude that the magma source of the volcano is not a limiting factor for the eruption rate or the longevity of the eruption.

For example, if we assume that 10% of the minimum estimated subcrustal melt will erupt, then the total eruptive basaltic material will be of the order of 1 km^3 and the eruption could last for 2-3 years at the present eruption rate. But of course, these estimates are highly uncertain. For comparison, the estimated volume of a similar eruption 14.100 years ago (Sæmundsson and Sigurgeirsson, 2013), is about 5 km^3. This former eruption, which formed the Thráinsskjöldur shield volcano at the northern flanks of Fagradalsfjall with an eruptive crater almost above the northern part of the 2021 magma dyke, could have lasted more than 10 years if the eruption rate were on the same order as in 2021.

Reference:

Self, S., Thordarson, Th. & Mike Widdowson, M. Gas Fluxes from Flood Basalt Eruptions. *Elements*, **1**, 283–287, (2005).

Sæmundsson, K., & Sigurgeirsson, M.Á. Reykjanesskagi. In Sólnes J. et al. (ed), Náttúruvá á Íslandi, *Viðlagatrygging Íslands/Háskólaútgáfan*, 379—401 (2013).